Synergetic control of band gap and structural transformation for optimizing TiO$_2$ photocatalysts

Heechae Choi [a,b,1], Sovann Khan [c,d,1], Junghyun Choi [e], Duong T.T. Dinh [c,d], Seung Yong Lee [c,d], Ungyu Paik [e], So-Hye Cho [c,d,*], Seungchul Kim [a,d,*]

[a] Computational Science Research Center, Korea Institute of Science and Technology, 02792, Republic of Korea
[b] Center of Materials Simulation Research, Virtual Lab Inc., 02792, Republic of Korea
[c] Materials Architecturing Research Center, Korea Institute of Science and Technology, 02792, Republic of Korea
[d] Department of Nanomaterials Science and Engineering, Korea University of Science and Technology, Daejon, 34113, Republic of Korea
[e] Department of Energy Engineering, Hanyang University, Seoul, 04763, Republic of Korea

ARTICLE INFO

ABSTRACT

Impurity doping and synthesizing polymorphic particles are the common strategies to improve activity of TiO$_2$ photocatalyst by lowering the band gap and enhancing electron-hole separation rate. However, these two approaches have side effects. Doping of impurities make space charge region (SCR) thinner near the surface, which requires smaller sized particles than undoped TiO$_2$ for the optimal performance. Polymorphic TiO$_2$ particles, in which rutile and anatase phases coexist in a particle, are usually large due to energetic unstability of the rutile phase in a fine particle. For this contradiction that one needs small size while the other needs large size, two effects are not easy to be combined. In this study, we suggest a *dual-doping* strategy to solve the contradictory problem of SCR reduction by donor doping and inevitable size growth in polymorphic particles. We successfully dope W, a band gap narrower, into fine size of polymorphic particles by Sn-codoping, a promoter of the anatase-to-rutile transformation (ART), and demonstrate greatly improved photocatalytic activity. The accelerated ART by Sn-doping could keep the size of polymorph junctioned TiO$_2$ small ($\sim$10 nm) as lower temperature annealing become able to induce the ART. The concept of dual doping with a band gap narrower and an ART promoter provides a way to synthesize highly active photocatalysts by overcoming the drawback from shortened SCR length.

© 2017 Elsevier B.V. All rights reserved.

1. Introduction

Anatase TiO$_2$, an extensively used photocatalyst material, is becoming increasingly important due to the rapidly growing global demands for sustainable, clean energy resources, and water/air purification technology using solar energy [1–6]. A number of engineering efforts have been devoting to overcoming the notorious weak points of the wide band gap (3.2 eV) and low electron-hole separation rate [4–11].

The first widely used approach is impurity doping to lower the band gap and to enhance photo-absorption [11–18]. Ideally, impurities should induce new bands close to the edges of valence bands (VB) and/or co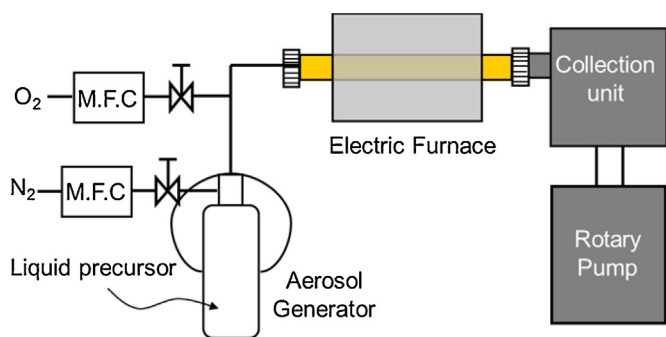nduction bands (CB), to narrow the band gap of TiO$_2$ [5,13,17]. Such shallow levels prevent Shockley-Read-Hall recombination [19] so that the carrier lifetime is not shortened. A side effect of impurity doping is the decrease of the space charge region (SCR) near the surface, where photo-excited electrons and holes separate. This effect leads to the utilization of a smaller fraction of the TiO$_2$ particles. However, if particles are too small (e.g. smaller than 10 nm), sufficient amount of band bending does not appear [6]. Therefore, it is desirable to synthesize particles of which size fits to the SCR to keep the proper effect of doping of band gap narrower while suppress its side effects.

The second approach is making polymorphic TiO$_2$ particles, in which rutile and anatase phases co-exist in a particle [20–31] to enhance electron-hole separation rate. Photo-excited electrons and holes are separated at both the SCR near the surface and at the polymorphic junction between the rutile and anatase phases, leading to the achievement of a higher electron-hole separation rate. The typical method of synthesis for partial transformation to rutile is by annealing the as-synthesized anatase powder at a high temperature ($\gtrsim$600 °C) [21,28–31].

* Corresponding authors at: Computational Science Research Center, Korea Institute of Science and Technology, 02792, Republic of Korea
E-mail addresses: sohyec@kist.re.kr (S.-H. Cho), sckim@kist.re.kr, k.seungchul@gmail.com (S. Kim).
[1] These authors contributed equally to this work.

Scheme 1. Schematic diagram of CVS (Chemical Vapor Synthesis) apparatus.

Table 1
Band gaps of doped and undoped TiO_2, calculated using the HSE06 method. The experimental band gaps of undoped anatase and rutile are 3.20 eV (388 nm) and 3.03 eV (409 nm), respectively. Numbers in the square brackets are the corresponding wavelengths, in units of nm.

	TiO_2	TiO_2:Sn	TiO_2:W
Anatase	3.25 [382]	3.25 [382]	3.20 [388]
Rutile	2.92 [425]	2.87 [432]	2.56 [484]

Effects of donor-doping and polymorphic junction might be able to combine if donors are doped into polymorphic TiO_2 particles. In theory, to drive the combined effects the size of particle should be kept smaller than the optimal size of undoped TiO_2 particles due to the shortened SCR by donors. However, high-temperature annealing for polymorphic junction formation inevitably causes substantial growth of particles [28,32–35]. For this reason, the fraction of the rutile phase and particle sizes are hardly controlled at the same time. Thermal engineering of the undoped anatase TiO_2 for photocatalyst mostly relies on experience, and the best photocatalytic activity is known to occur with rutile phase fraction of 25–30 mol% [5,20].

In this study, we have successfully improved photocatalytic activity by both narrowing the band gap and inducing a partial anatase-to-rutile transformation (ART) in fine TiO_2 particles of ~10 nm, using two types of dopants. Tungsten (W) has been studied as a dopant for TiO_2 by our group [36] and others as well [37–39] in an effort to increase its photocatalytic activity under the visible light (presumably, by the effect of band gap narrowing) while tin (Sn) is known to promote ART [40]. Therefore, the band gap narrowing was attempted with W dopants and formation of polymorphic TiO_2 particles of extremely small size was aimed with Sn dopants. Indeed, it was expected that Sn does not induce any deep level in the gap as its oxidation state is the same as that of Ti. With Sn as an ART promoter, we were able to make polymorphic TiO_2 nanoparticles by annealing at a low temperature or for a shorter time than without Sn, thus restricting their size growth; we synthesized ~10 nm anatase-rutile mixed-phase particles at 550 °C, achieving a higher photocatalytic activity by a factor of 1.67 compared to a commercial photocatalyst, P25. This study also demonstrates that an efficient electron-hole separation in fine particles (~10 nm) is important to provide a high photocatalytic activity.

2. Experimental and computational methods

2.1. Experiments

TiO_2 nanoparticles were synthesized by chemical vapor synthesis (CVS) [36]. Details of the experimental setup are described in Scheme 1. Metal propoxides, such as titanium tetra-isopropoxide (TTIP, 98%, Junsei, Japan), tungsten (VI) isopropoxide (Alfar Aesar, 5% w/v in isopropanol), and tin (IV) isopropoxide (Alfar Aesar, 10% w/v in isopropanol) were well-mixed in solution and atomized by an aerosol generator with N_2 gas. The alkoxide aerosol was delivered with N_2 gas, mixed with O_2 gas, and passed through a tube furnace that was preheated at 1350 °C. Along a hot tube furnace, the aerosol precursor underwent thermal decomposition to form nanoparticles. Finally, the produced particles were collected at a thermophoretic particle separator. Gas flow rates were fixed at 5 slm for N_2 and 4 slm for O_2. The amount of the tungsten precursor was adjusted to be 1 mol% of the amount of the titanium precur-

sor, while the amount of the tin precursor was varied from 0.3 to 3 mol% of that of the titanium precursor. The W-doping amount was fixed to 1 mol% since it gave the optimal photocatalytic activity as reported previously [36]. A kinetic study of the anatase-rutile transformation was conducted by annealing the as-prepared sample at different temperatures (500–700 °C) under ambient conditions.

Characterizations of TiO_2 powder were conducted by X-ray diffraction (XRD) (D8 Advanced, Brucker Corporation); transmission electron microscopy (TEM) and small area electron diffraction (SAED) (Tecnai, FEI Company, USA); and UV–vis spectrophotometry (Varian Cary 100, Agilent Technologies, USA). From XRD spectra, the particle size of TiO_2 was calculated by the Debye–Scherrer equation [41], and the fractions of anatase and rutile were calculated, respectively, by integrating the (1 0 1)-anatase peak and (1 1 0)-rutile peaks [42]. The Mott-Schottky plot was measured at a frequency of 100 Hz, using a potentiostat (PGSTAT 302N, Autolab, Netherlands). 0.5 M Na_2SO_4 solution was served as an electrolyte. Photocatalytic activities of TiO_2 powder were determined from the degradation of methylene blue (MB) under visible light. 20 mg of TiO_2 powder was mixed with 50 mL of MB (5×10^{-4} wt%, Sigma Aldrich) under dark conditions for 60 min. 5 mL of this mixture was poured into a glass tube and irradiated by a metal-halide lamp (Osram, HQI-TS/NDL, 150 W, irradiation wavelength = 370–800 nm) without using a UV cut-off filter. After a predetermined time, the irradiated MB solution was centrifuged (13,500 rpm) to remove particles. The MB remaining after photocatalytic degradation was determined by UV–vis absorption at λ = 664 nm, and calculated based on the calibration curve made with a reference MB solution [43].

2.2. Computational methods

The doping energies of Sn and W for rutile and anatase were calculated using Eqs. (1) and (3). The total energy terms in Eq. (1) were calculated using density functional theory (DFT) [44,45] calculations within the generalized gradient approximation (GGA-PBE [46,47]) plus Hubbard U (U_{Ti-3d} = 4.0 eV and U_{Sn-4d} = 3.5 eV) [48], using the VASP software [49]. A projector-augmented wave (PAW) [50,51] was used, with a wave function cut-off of 400 eV and $4 \times 4 \times 4$ Brillouin zone sampling [52] for the structural relaxation. The HSE06 functional [53], with $2 \times 2 \times 2$ Brillouin zone sampling, was used to calculate the electronic density of states (DOS) of the atomic structure obtained from the PBE + U calculation. The formation energies of TiO_2, WO_3, and SnO_2, and lattice constants obtained using PBE + U (U = 4.0 and 2.7 eV for Ti-3d and W-5d) calculations are very close to the experimental values. The HSE06 method gives the accurate band gap for anatase and rutile TiO_2 (Table 1).

Periodic supercell model structures of $3 \times 3 \times 1$ and $2 \times 2 \times 3$ primitive unit cells were used for the bulk anatase and rutile, respectively. These sizes were chosen following suggestions from careful convergence tests of previous DFT works [18,54]. The position of each atom as well as the supercell vectors were relaxed. The doping energies (ΔE) of W and Sn were calculated with a varying charge q, using the equation [55–57],

$$\Delta E_{Dq}(T, P) = E_{Dq} - E^0 - \sum_{\alpha} n_\alpha \mu_\alpha(T, P) + q(E_v + \Delta V + E_F) \qquad (1)$$

E_{D^q} is the total energy of the TiO$_2$ supercell with the dopant D and net charge q; E^0 is the total energy of the defect-free TiO$_2$; μ_α is the chemical potential of the element α added to or removed from the supercell to generate D; n_α is the number of α atoms involved in the dopant structure; E_v is the valence band maximum (VBM) of the defect-free TiO$_2$; ΔV is the shift of the VBM in the defective cell by the dopant, relative to that in the defect-free TiO$_2$; E_F is the Fermi level referenced to E_v. The net charge q is +2 when W^{6+} replaces Ti^{4+} (i.e., W$_{Ti}{}^{2+}$).

The environmental conditions were considered using the chemical potential of oxygen (μ_O), while thermal energies of the solid phases were ignored. The ideal gas approximation was applied to determine the chemical potential of oxygen:

$$\mu_O \left(T, P_{O_2} \right) = \frac{1}{2} \left\{ \tilde{\mu}_{O_2} \left(T, P^\circ_{O_2} \right) + k_B T \ln \left(\frac{P_{O_2}}{P^\circ_{O_2}} \right) \right\} \tag{2}$$

where $\tilde{\mu}_{O_2} \left(T, P^\circ_{O_2} \right)$ is the chemical potential of O$_2$ at standard pressure ($P^\circ_{O_2} = 0.21$ atm) and the given temperature T [58]. The experimental binding energy of an oxygen molecule, 2.56 eV/atom [59], was used.

Doping energy from the PBE + U calculations was further corrected by extrapolating the change of the crossing point of ΔE_{D^q} and $\Delta E_{D^{q'}}$ in the PBE and PBE+U calculations [51],

$$\varepsilon \left(q/q' \right) = \varepsilon \left(q/q' \right)^{PBE+U} + \frac{\Delta \varepsilon}{\Delta E_g} \left(E_g^{exp} - E_g^{PBE+U} \right) \tag{3}$$

with

$$\frac{\Delta \varepsilon}{\Delta E_g} = \left(\frac{\varepsilon \left(q/q' \right)^{PBE+U} - \varepsilon \left(q/q' \right)^{PBE}}{E_g^{PBE+U} - E_g^{PBE}} \right), \tag{4}$$

where $\varepsilon \left(q/q' \right)$ is the crossing point of ΔE_{D^q} and $\Delta E_{D^{q'}}$. E_g^{exp}, E_g^{PBE+U}, and E_g^{PBE} are the band gap energies obtained from the experiments, PBE + U and PBE, respectively.

Because the oxidation state of W is different from that of Ti, O can be incorporated into the TiO$_2$ lattice (O$_i{}^{2-}$, interstitial oxygen) to compensate W^{6+} at the Ti^{4+} site, according to either of the following possible reactions,

$$WO_{3(s)} + Ti^{4+} + \Delta E \rightarrow W_{Ti}{}^{2+} + TiO_2 + 2e^- + \tfrac{1}{2}O_{2(g)} \tag{5}$$

$$WO_{3(s)} + Ti^{4+} + \Delta E \rightarrow W_{Ti}{}^{2+} + TiO_2 + O_i{}^{2-} \tag{6}$$
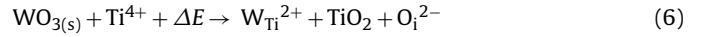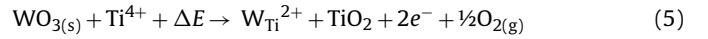
The doping energy of W depends on the chemical potential of oxygen, while that of Sn does not since the oxidation state of Sn is the same as that of Ti. WO$_3$ and SnO$_2$ were used as reference materials of W and Sn for calculation of doping energies.

3. Results and discussions

3.1. Structural and morphological characterizations of TiO$_2$ nanoparticles

DFT calculations predict that the substitutional doping energies of Sn are −0.17 eV/atom in rutile and 0.35 eV/atom in anatase, indicating that Sn promotes the ART thermodynamically. The most stable structure of Sn doping is predicted to be the substituting Ti site (Sn$_{Ti}$) without extra charge regardless of the Fermi level. However, the doping energy and charged state of W varies, depending on the Fermi level of TiO$_2$. For this work, 1.0 mol% of W-doping is employed according to our previous work for W-doped TiO$_2$ for photocatalysis [36]. The optimal doping concentration of W toward the photocatalytic performance could be different when it is codoped with Sn. However, we do not explore dependence of the catalytic activity on the W amount because optimizing W concentration is not the purpose of this study. We also expect that optimal concentration is not changed much by Sn dopants as Sn does not change the band gap, from our simulations and photoabsorption spectra presented in this report, and does not donate any electron or hole as its oxidation state is the same as Ti.

Sn promotes the formation of the rutile phase in anatase particles, as displayed in Fig. 1(a), in which a stronger rutile signal appears for Sn^{4+}-doped samples than for pure and W-doped samples. Every sample was annealed at 600 °C for 1 h because the crystallinity of the as-prepared samples was too low for compar-
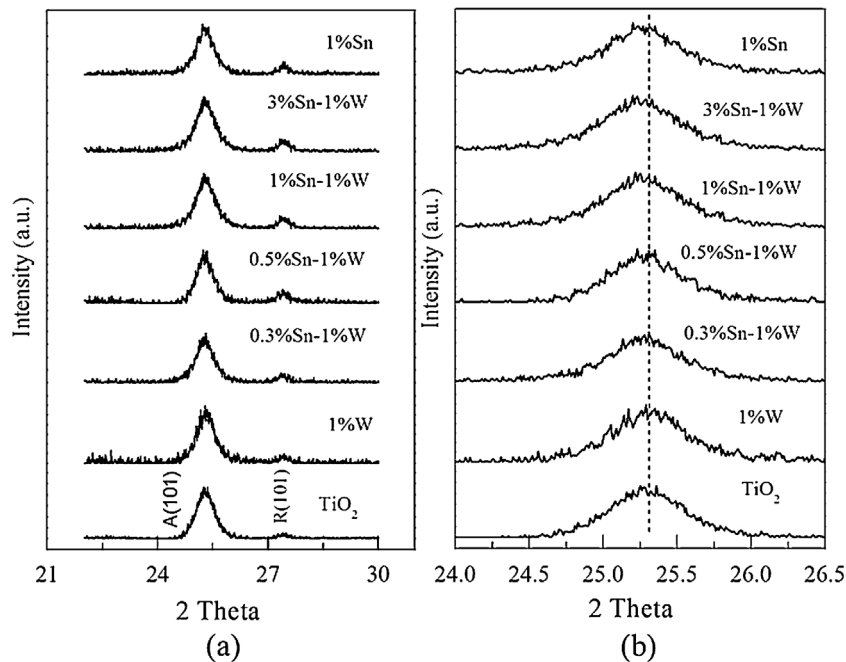

Fig. 1. (a) Long-range XRD and (b) slow-scanned XRD of TiO$_2$ undoped, singly-doped with 1 mol% W or 1 mol% Sn, and codoped with 1 mol% W and various Sn concentration (0.3–3 mol%). All samples were annealed at 600 °C for 1 h before the measurement.
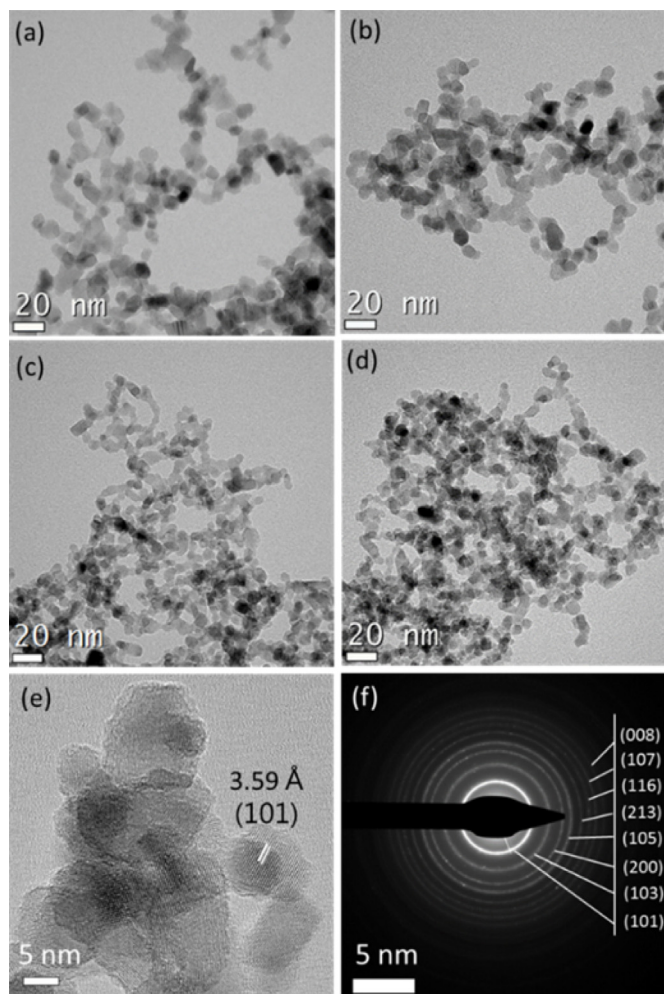
Fig. 2. TEM images of (a) undoped TiO_2; (b) TiO_2:W; (c) TiO_2:W–Sn and (d) TiO_2:Sn, (e) an high-resolution image of TiO_2:W–Sn, and (f) a SAED pattern of TiO_2:W–Sn.

Fig. 3. Size distributions of (a) undoped TiO_2, (b) TiO_2:W, (c) TiO_2:W–Sn, and (d) TiO_2:Sn, obtained from TEM images.

crystals. The ring pattern matches very well to planes of anatase TiO_2 which is the major phase of the TiO_2:W–Sn sample.

We measured the particle sizes of 100 particles from TEM images of each sample of different doping, and summarized the results in Fig. 3. Average particle sizes of undoped and W-doped TiO_2 are 14.09 ± 0.28 nm and 13.43 ± 0.22 nm, and those of Sn-doped and Sn-W codoped TiO_2 are 10.83 ± 0.21 nm and 11.46 ± 0.19 nm, respectively. Since the nanoparticles are well crystalized, these measured values are quite similar to the calculated values using Debye–Scherrer equation [41] with the full widths at half maxima (FWHM) of antatase (101) peak of XRD data in Fig. 1(b) (15.06 nm for undoped; 13.56 nm for W-doped; 9.52 nm for Sn-doped; and 9.04 nm for W-Sn codoped TiO_2). Interestingly, the sizes calculated with anatase (101) XRD peak of Sn-containing samples are smaller than ones from TEM images while others are almost the same or larger. In spite of having errors in size estimation from both methods, it can be understood that the sizes of Sn-containing particles calculated by the Debye-Scherrer equation is smaller than those by TEM images because they contain large portion of rutile phase, thus difference in size estimation from two methods is an evidence of synthesizing ~10 nm polymorphic particles; XRD peak of anatase informs size of anatase phase only while TEM shows whole particles.

3.2. Chemical characterizations of TiO_2 nanoparticles

To verify homogeneous mixing of W and Sn in TiO_2 by doping rather than physical mixing of oxide species (e.g., W-oxides and Sn-oxides), STEM and mapping images of each element are obtained and shown in Fig. 4. The mapping image of the element Ti perfectly matches with the STEM image while mapping images of the elements Sn and W are not clearly but just roughly matched. The signals of Sn and W are low due to their low doping concentration (1 mol% each with respect to total metal amounts). Spread elemental mapping indicates that the separate oxide species are not likely formed.

Our simulations predict the oxidation states of W and Sn are 6+ and 4+, and we use these oxidation states to interpret all our results. However, the oxidation states of them can vary in general [37], and

ison. An increase in the rutile-phase fraction was observed with respect to the amounts of Sn^{4+}-doping up to 3.0 mol%, but higher doping concentration is not presented here since it causes the formation of SnO_2 impurity phase (see Fig. S1 in the Supplementary Materials for XRD data of Sn doping concentration of 5 mol%). Therefore, a maximum of 3 mol% of Sn^{4+}-doping was used for photocatalytic experiments. The slow-scanned XRD peaks of plane (101) exhibit no significant change of the peak position with W-single doping while a small shift to a lower angle with both Sn-single doping and W-Sn codoping (Fig. 1(b)). This shift of peak position might be due to larger radius of Sn^{4+} (0.69 Å), while the radius of W^{6+} (0.60 Å) is very similar to Ti^{4+} (0.605 Å) [37,40].

Structural properties of the TiO_2 samples were analyzed by TEM (Fig. 2) after annealing at 600 °C for 1 h. The image of undoped TiO_2 shows a very fine particle size and a facetted morphology which is a distinctive of single-crystalline TiO_2 particles (Fig. 2(a)). The size and shape of W-singly doped sample (Fig. 2(b)) are very similar to the undoped sample while particle sizes of Sn-singly doped and W-Sn codoped samples (Fig. 2(c) and (d)) are little smaller than those of the undoped sample. A high-resolution TEM image of W-Sn codoped TiO_2 in Fig. 2(e) shows a well-defined lattice distance of 3.59 Å of (101) plane which is a little longer than that of pure anatase (3.52 Å), indicating elongation of lattice by Sn as it is also observed in Fig. 1(b). A clear ring pattern is observed in Fig. 2(f) by SAED inferring that the sample is composted with very small sized
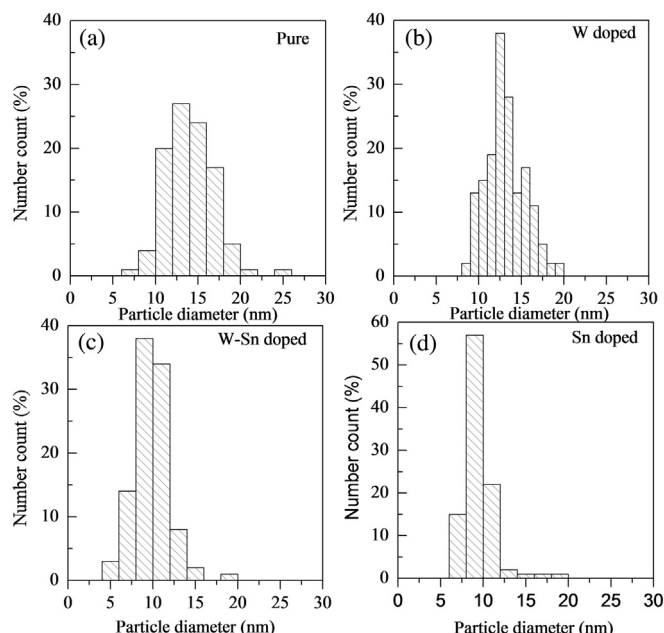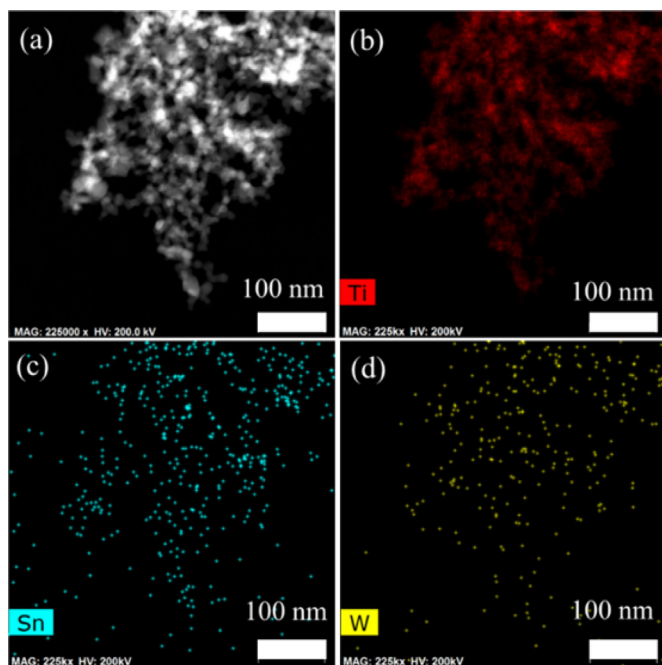
Fig. 4. (a) An STEM image and mapping images of elemental (b) Ti, (c) Sn, and (d) W of $Ti_{0.98}O_2$:$W_{0.01}$-$Sn_{0.01}$ annealed at 600 °C for 1 h.

Fig. 5. High-resolution XPS spectra of W $4f$, Sn $3d$, Ti $2p$, and O $1s$. Peaks appear at 35.48 eV (W^{6+} $4f_{7/2}$), 37.78 eV (W^{6+} $4f_{5/2}$), 486.47 eV (Sn^{4+} $3d_{5/2}$), 494.87 eV (Sn^{4+} $3d_{3/2}$), 458.61 eV (Ti^{4+} $2p_{3/2}$), 464.41 eV (Ti^{4+} $2p_{1/2}$), and 529.88 eV (lattice O^{2-} $1s$).

hence we confirm the oxidation states using an XPS analysis of our TiO_2 samples. Fig. 5 shows high-resolution XPS data of W $4f$, Sn $3d$, Ti $2p$ and O $1s$. Deconvolution of W $4f$ and Ti $3p$ peaks at 37.08 eV reveals having $4f_{7/2}$ and $4f_{5/2}$ of W^{6+}. Notably, at the present concentration of W doping, 1 mol%, no other oxidation state is found [36]. Only in the Sn-containing samples, unique binding energies of $3d_{5/2}$ and $3d_{3/2}$ of Sn^{4+}, are observed at 486.47 eV and 494.87 eV. Electron binding energies in Ti^{4+} are observed at 458.61 eV and 464.41 eV, which respectively correspond to Ti $2p_{3/2}$ and Ti $2p_{1/2}$ with no trace of binding energies of Ti^{3+}. Binding energies of O $1s$ are found for three different species: the lattice oxygen (O_{Ti-O}); the surface hydroxyl oxygen (O_{O-H}); and the chemisorbed oxygen (O_{O-O}) species. A strong peak picking at 529.88 eV corresponds to the lattice oxygen, and a broad peak at 531.16 eV is related to surface oxygen (O_{O-H} and O_{O-O}) [17].

3.3. Quantitative analysis of the ART by Sn doping

From the XRD data given in Fig. 1(a), fractions of rutile phase in each TiO_2 sample annealed at 600 °C are extracted and compared with those in samples annealed at different temperatures, 500–700 °C, for 1 h (see Fig. S2 in the Supplementary Materials for XRD data of samples annealed at different temperatures). Plots of rutile amounts as a function of annealing temperatures for four different samples (undoped, W-doped, Sn-doped, and W-Sn codoped TiO_2) are represented in Fig. 6(a). It appears that no rutile phase is formed in all samples at 500 °C, but, at 550 °C, only Sn-containing samples shows the evolution of rutile phase (5.1% and 7.5% of rutile fraction in W-Sn-codoped and Sn-doped TiO_2 samples, respectively). With further increment of the annealing temperature, the difference in the rutile fraction by Sn doping became larger, indicating that the Sn dopant functions as an ART promoter, regardless of the presence of the secondary dopant W^{6+}., It is more clearly visualized in the plot of the relative growth of particle (Fig. 6(b)) that the particle size is controlled to be much smaller at the same degree of anatase/rutile polymorphic junction when Sn is doped. See Table S1 in the Supplementary Materials for the calculated particle sizes from XRD data. It is worth noting that the ART and growth of particle
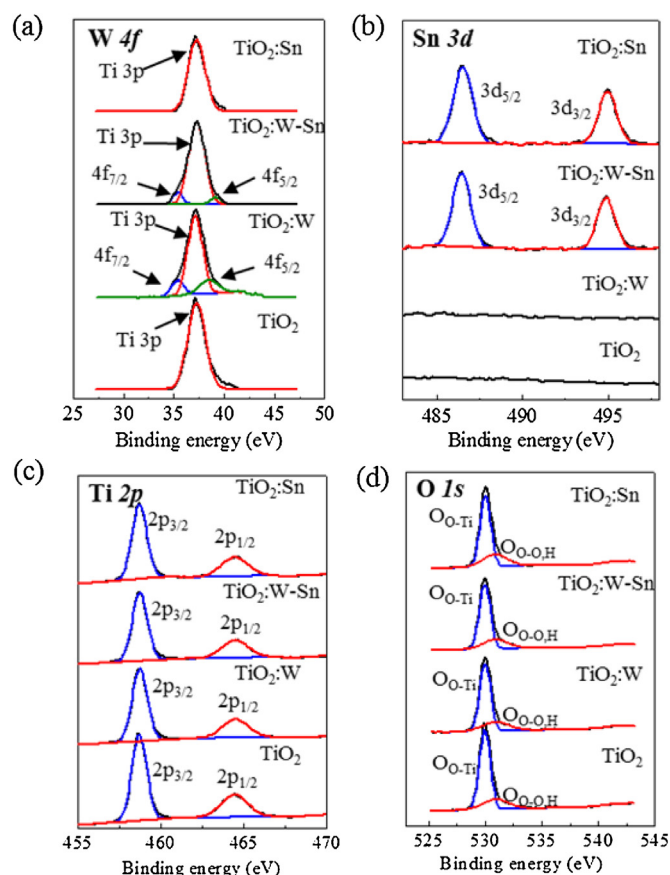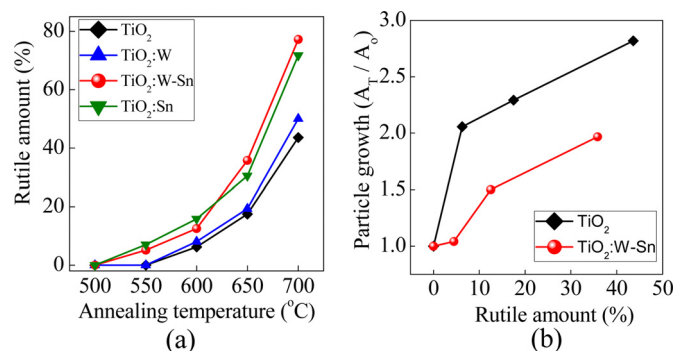

Fig. 6. (a) Fraction of rutile phase in TiO_2 (%) as a function of annealing temperature (500–700 °C) and (b) relative growth of particle size at an annealing temperature T as a function of rutile amount (%). Concentrations of Sn and W are 1 mol% each for all samples, and the samples were annealed for 1 h at the designated temperature. A_o and A_T are particle sizes of as-synthesized samples and annealed samples at a temperature T, respectively.

cle size typically occur concomitantly, especially when particles are extremely fine (i.e., <20 nm) [27]. Therefore, Sn doping is an effective way to control the particle size while obtaining the desired anatase-to-rutile ratio.

The effect of Sn on the ART was investigated more quantitatively by tracking the amount of anatase phase transformed to the rutile phase. Assuming that the rate of transformation of nanocrystalline anatase TiO_2 to the rutile phase is of the nth order with respect to the
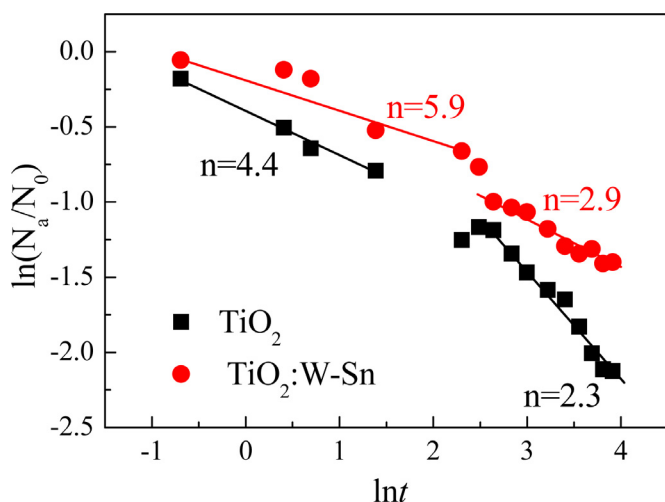
Fig. 7. Rutile phase formation with annealing time at 650 °C. N_0 is the initial number of anatase particles, N_a is the effective number of anatase particles and t is annealing time in hour.

number of anatase particles [27], the rate of ART can be expressed as:

$$-\frac{d(N_a/N_0)}{dt} = k_1(N_a/N_0)^n \qquad (7)$$

where k_1 is the rate constant of transformation and N_0 is the initial number of anatase particles. N_a is the effective number of anatase particles, which is defined in terms of the total amount of anatase phase as $4/3\pi R^3 N_a$, where R is the average radius of particles, calculated from the FWHM of XRD data [27].

The doped sample shows a higher order of reaction in both initial and final stages of transformation (Fig. 7), which means that faster transformation occurs in the doped sample. The initial and late stages show different orders of reaction, n, in both pure and doped TiO_2, which is similar to the previous experimental observations [31]. Undoped TiO_2 has $n = 4.4$ in the initial stage and $n = 2.3$ in the later stage of rutile transformation. The promotion of the ART by Sn will promote not only interface nucleation (i.e., the initial stage) but also bulk transformation (i.e., the final stage), which is rarely observed without dopants [27].
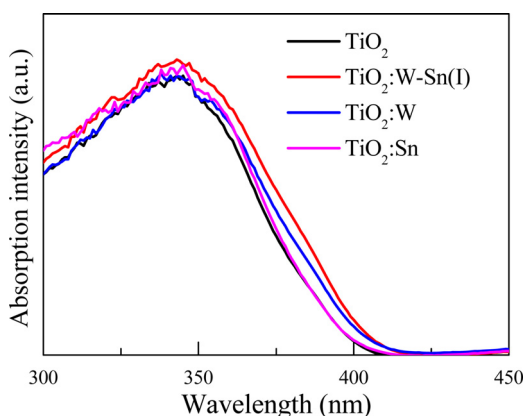

Fig. 8. UV–Vis absorption spectra of undoped, W-doped, Sn-doped, and W-Sn-codoped TiO_2.

3.4. Optical properties and electronic structure of W-Sn codoped TiO_2 nanoparticles

Fig. 8 displays the absorption spectra of TiO_2 nanoparticles annealed at 600 °C for 1 h. Compared to the undoped TiO_2, W-doped and W-Sn codoped samples absorb more photons in the 350–410 nm range while the Sn-doped sample shows negligible changes. Interestingly, W-Sn codoping provides higher absorption than W-doping, although Sn does not narrow the band gap. We attribute this phenomenon to the presence of larger portion of the rutile phase in codoped samples. Sn-doping increases photon absorption <350 nm for both Sn-doped and W-Sn codoped samples, which might be because of the increased density of states (DOS) in the conduction band (3.5–4.0 eV from VBM) of Sn-doped rutile TiO_2 (Fig. 9d).

The electronic DOS from the HSE06 calculations explains the change of absorption spectra. W^{6+}-doping causes a very small reduction in the band gap of anatase, as the d-states of W^{6+} have a long tail down to only 0.05 eV below the CBM (Fig. 9(a)). On the other hand, W^{6+} in rutile has a main peak of d-orbital states below the CBM (Fig. 9(b)), and provides a much larger band gap reduction (0.36 eV). Sn^{4+}-doping causes almost no reduction in the band gap of both rutile and anatase (Fig. 9(c) and (d)). The band gaps of doped and undoped TiO_2 are summarized in Table 1.

Our calculations suggest that the enhanced intensity of photo-absorption of the W-Sn codoped sample is mainly caused by the larger fraction of the rutile phase, as a significant reduction of the band gap is caused by the W^{6+}-dopant in the rutile phase, and the substantial increase in DOS appears only at the CB of W-doped rutile. However, as shown in the following session, the improvement in photocatalytic activity is much greater than that in absorption, indicating there is another factor besides the absorption efficiency.

We performed Mott-Schottky measurements on W-Sn codoped TiO_2 powder to check whether band edges are insensitive to doping or not (Fig. 10). A positive slope indicates that the sample is n-type, and CBM approximates the flat band potential for the n-type semiconductor. Codoped TiO_2 shows two flat band potentials at −0.72 eV and −0.74 eV, which correspond to the CBMs of anatase and rutile phases, respectively (Fig. 10(a)) [53]. The CBM offsets of pure and W-Sn codoped TiO_2 were measured to be 0.11 eV and 0.02 eV, respectively. The decrease of offset is due to the band gap reduction of the rutile phase by W^{6+}-doping. It was found that the band positions of TiO_2 particles are not significantly changed by Sn^{4+}- or W^{6+}-doping. A minor change was observed for the rutile phase, which showed a small reduction of the band gap from 3.0 to 2.9 eV. This is in good agreement with our electron DOS calculations shown in Fig. 9. Based on these results, the proposed band alignment of W-Sn codoped TiO_2 is presented in Fig. 10(b). The band alignment shows that the photo-excited electrons and holes will transfer to the CB of anatase and VB of rutile, respectively.

3.5. Photocatalytic activity of W-Sn codoped TiO_2 nanoparticles

In Fig. 11, the photocatalytic degradations of methylene blue (MB) by six different TiO_2 samples are compared. Commercially available P25 (Evonik-Degussa, Germany) was used as a reference. The undoped (TiO_2), W-doped (TiO_2:W), Sn-doped (TiO_2:Sn), and W-Sn-codoped (TiO_2:W-Sn(I)) samples were annealed at 600 °C, while TiO_2:W-Sn(II) was annealed at 550 °C. For a systematic understanding of the observed photocatalytic activities of different TiO_2 samples, the rate constants were obtained from the slope of $\ln(C_0/C)$ as a function of time and are listed in Table 2 along with the fraction of the rutile phase and the size of particles. The W-Sn codoped sample showed the best performance, followed by the W-doped, Sn-doped, and pure TiO_2 samples, in that order. All
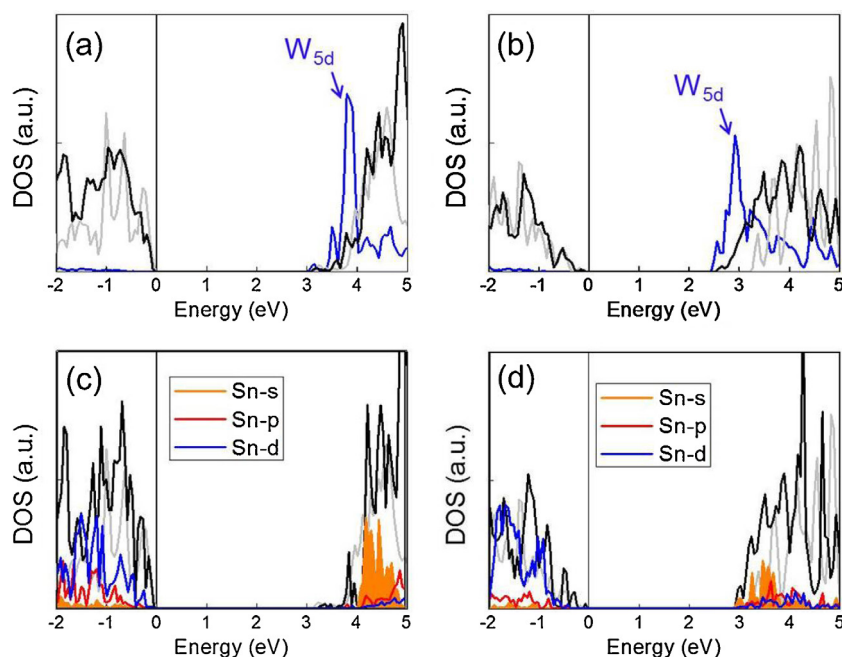
Fig. 9. Calculated electronic DOS of W^{6+}-doped (a) anatase and (b) rutile, and Sn^{4+}-doped (c) anatase and (d) rutile. The HSE06 functional is used. The black curves are the normalized total DOS of doped TiO_2, and the grey curves are those of undoped TiO_2. DOS of the Sn s-orbital is shown by the filled orange curve. (For interpretation of the references to colour in this figure legend, the reader is referred to the web version of this article.)
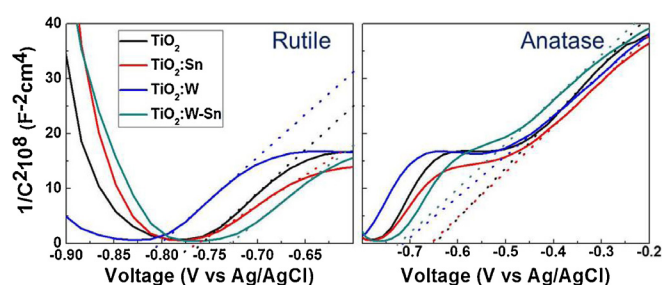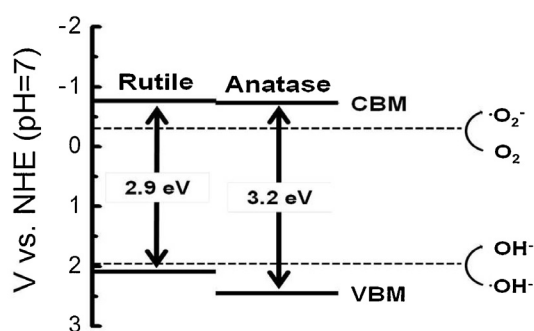
Fig. 10. (a) Mott-Schottky curves for undoped, Sn-, W-, and W-Sn doped TiO_2 with best photocatalytic activities and (b) the estimated band positions of anatase and rutile phases of W-Sn codoped TiO_2 nanoparticles. The intersects of the dotted lines and tangents of the curves in the left and right panels of (a) indicate the band positions of rutile and anatase phases of TiO_2 nanoparticles, respectively.

Fig. 11. Photocatalytic degradations of MB by undoped and doped TiO_2 nanoparticles under the irradiation wavelength of 370–800 nm (by a metal halogen lamp). C_0 is the initial MB concentration and C is the concentration after the reactions. W-Sn codoped (II) was annealed at 550 °C while all other samples were annealed at 600 °C except P25. Slopes of lines are reaction constants, k. Each data point was obtained from three repeated experiments and the error range is within 5%.

Table 2
Rutile fractions, particle sizes, rate constants, and band gaps of TiO_2 particles. The W-Sn-codoped (II) sample was annealed at 550 °C while all others were annealed at 600 °C. Numbers in the square brackets of size are the ones measured using TEM images.

Samples	Rutile fraction (%)	Size (nm)	Rate const., k(min^{-1})	Band gap (eV)
P25	33.33	25–85	0.0385	3.1
TiO_2	6.28	15.06 [14.09]	0.0183	3.1
TiO_2:Sn	13.50	9.52 [10.83]	0.0475	3.1
TiO_2:W	7.50	13.56 [13.43]	0.0585	3.0
TiO_2:W–Sn (I)	12.53	9.04 [11.46]	0.0643	2.9
TiO_2:W–Sn (II)	5.10	8.72	0.0630	3.0

the doped samples showed better activity than the P25 reference. In particular, the codoped sample showed a higher activity than this commercial photocatalyst by the factor of 1.67.

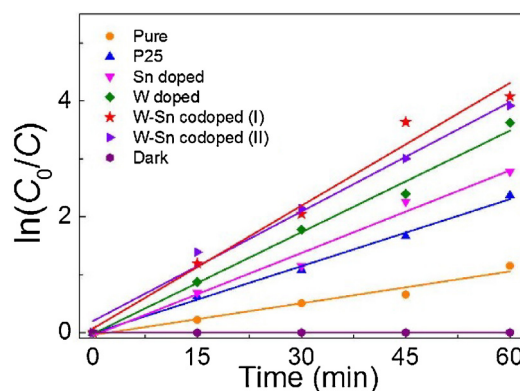The undoped TiO_2 sample shows the lowest photocatalytic reaction constant (47% of that of P25). The depletion region of undoped TiO_2 with a space charge of $10^{18}|e|/cm^3$, which is frequently observed natural concentration by oxygen vacancies, is approximately 50 nm [5,6]. This is larger than the radius of undoped

TiO_2. Hence, the band bending of undoped TiO_2 particles, for which the fraction of the anatase phase is 93.72%, is expected to be smaller than that of doped or larger particles. In addition, the smaller fraction of the rutile phase of the undoped TiO_2 sample might be the reason for lower activity; more electron-hole pairs are separated at the polymorph boundary in P25. The Sn-doped sample, whose rutile fraction is much smaller than P25, shows a higher reaction constant than P25 by 23%. It is not clear why Sn-doped sample shows higher activity than P25, but a possible reason is that more electrons and holes can be driven to the surface before relaxation to the band edges, i.e., hot-carrier transport, for Sn-doped sample due to its much smaller size.

Notably, the improvement of the photocatalytic activity by W doping is much greater than the increase of the photo-absorption, which may result from increased built-in electric field in depletion region by the charged impurity, W^{6+}. Undoped and W-doped samples have very similar fractions of the rutile phase and particle sizes. TiO_2:W absorbs more photons as its band gap is smaller by 0.1 eV. However, the reduction of the band gap from 3.1 to 3.0 eV increases the photon absorption by approximately 14%, which is much smaller than the observed improvement in the photocatalytic activity (the rate constant of W-doped sample is higher than that of undoped one by a factor of 3.2). A hidden and significant impact of donor doping is the enhancement of drift velocity of charge carriers such that more photo-excited carrier arrived to the surface before recombination. The same interpretation is possible for TiO_2:Sn and TiO_2:W-Sn(I), the two samples with very similar rutile fractions and particle sizes.

TiO_2:W-Sn(II) shows that a highly active photocatalyst can be synthesized at a low temperature, with activity almost identical to that of the sample prepared at higher temperatures, namely, TiO_2:W-Sn(I). TiO_2:W-Sn(II) contains less rutile phase and smaller in size than TiO_2:W-Sn(I) due to the lower annealing temperature, but shows similar activity. Its smaller size is beneficial to photocatalysis, due to higher surface area and increased portion of charge depletion region, while a little larger band gap and smaller fraction of rutile phases are the opposite. Positive and negative factors in structural and electronic parts are cancelled with each other. The important point of TiO_2:W-Sn(II) is its lowered annealing temperature despite having similar activity to TiO_2:W-Sn(I). From the engineering point of view, lowering the annealing temperature by $50\,^{\circ}C$ is a great improvement since it can save a large amount of energy.

4. Conclusions

We successfully dope band gap narrower, W^{6+}, into very small (~10 nm) polymorphic TiO_2 particles by codoping an ART promoter, Sn^{4+}, and demonstrate that the photocatalytic activity of such codoped TiO_2 nanoparticles can be improved substantially so as to elevate the photo-absorption rate and separate electrons and holes more efficiently. We also find over-improvement in photocatalytic activity comparing to the improvement in photo-absorption, which can be interpreted as a result of the enhanced drift velocity of charge carriers by strengthened electric field in the depletion region by the charged impurities. The temperature to drive the adequate ART was lowered from $600\,^{\circ}C$ to $550\,^{\circ}C$ by the Sn doping while keeping high activity.

Acknowledgements

Appendix A. Supplementary data

Supplementary data associated with this article can be found, in the online version, at http://dx.doi.org/10.1016/j.apcatb.2017.04.020.

References

[1] A. Fujishima, K. Honda, Electrochemical photolysis of water at a semiconductor electrode, Nature 238 (1972) 37–38.
[2] M. Fujihira, Y. Satoh, T. Osa, Heterogeneous photocatalytic oxidation of aromatic compounds on TiO_2, Nature 293 (1981) 206–208.
[3] R. Asahi, T. Morikawa, T. Ohwaki, K. Aoki, Y. Taga, Visible-light photocatalysis in nitrogen-doped titanium oxides, Science 293 (2001) 269–271.
[4] F. Fresno, R. Portela, S. Suárez, J.M. Coronado, Photocatalytic materials: recent achievements and near future trends, J. Mater. Chem. A 2 (2014) 2863–2883.
[5] J. Schneider, M. Matsuoka, M. Takeuchi, J. Zhang, Y. Horiuchi, M. Anpo, D.W. Bahnemann, Understanding TiO_2 photocatalysis: mechanisms and materials, Chem. Rev. 114 (2014) 9919–9986.
[6] K. Ozawa, M. Emori, S. Yamamoto, R. Yukawa, S. Yamamoto, R. Hobara, K. Fujikawa, H. Sakama, I. Matsuda, Electron–hole recombination time at TiO_2 single-crystal surfaces: influence of surface band bending, J. Phys. Chem. Lett. 5 (2014) 1953–1957.
[7] J. Tao, T. Luttel, M. Batzill, A two-dimensional phase of TiO_2 with a reduced bandgap, Nat. Chem. 3 (2011) 296–300.
[8] L. Li, P.A. Salvador, G.S. Rohrer, Photocatalysts with internal electric fields, Nanoscale 6 (2014) 24–42.
[9] J. Yu, J. Low, W. Xiao, P. Zhou, M. Jaroniec, Enhanced photocatalytic CO_2-reduction activity of anatase TiO_2 by coexposed {001} and {101} facets, J. Am. Chem. Soc. 136 (2014) 8839–8842.
[10] S. Ida, A. Takashida, S. Koga, H. Hagiwara, T. Ishihara, Potential gradient and photocatalytic activity of an ultrathin p–n junction surface prepared with two-dimensional semiconducting nanocrystals, J. Am. Chem. Soc 136 (2014) 1872–1878.
[11] D.W. Kim, S.C. Riha, E.J. DeMarco, A.B.F. Martinson, O.K. Farha, J.T. Hupp, Greenlighting photoelectrochemical oxidation of water by iron oxide, ACS Nano 12 (2014) 12199–12207.
[12] Y. Kou, J. Yang, B. Li, S. Fu, Solar photocatalytic activities of porous Nb-doped TiO_2 microspheres by coupling with tungsten oxide, Mater. Res. Bull. 64 (2015) 105–111.
[13] K. Nakata, A. Fujishima, TiO_2 photocatalysis: design and applications, J. Photonchem. Photobiol. C: Photochem. Rev. 13 (2012) 169–189.
[14] R. Marschall, Semiconductor composites: strategies for enhancing charge carrier separation to improve photocatalytic activity, Adv. Funct. Mater. 24 (2014) 2421–2440.
[15] S.S. Thind, G. Wu, A. Chen, Synthesis of mesoporous nitrogen–tungsten co-doped TiO_2 photocatalysts with high visible light activity, Appl. Catal. B: Environ. 38 (2012) 111–112.
[16] C. Das, I. Paramasivam, N. Liu, P. Schmuki, Photoelectrochemical and photocatalytic activity of tungsten doped TiO_2 nanotube layers in the near visible region, Electrochim. Acta 56 (2011) 10557–10561.
[17] S. Khan, H. Cho, D.H. Kim, S.S. Han, K.H. Lee, T. Song, H.C. Choi, Defect engineering toward strong photocatalysis of Nb-doped anatase TiO_2: computational predictions and experimental verifications, Appl. Catal. B: Environ. 206 (2017) 520–530.
[18] H. Choi, D. Shin, B.C. Yeo, T. Song, S.S. Han, N. Park, S. Kim, Simultaneously controllable doping sites and the activity of a W-N co-doped TiO_2 photocatalyst, ACS Catal. 6 (2016) 2745–2753.
[19] W. Shockley, W.T. Read, Statistics of the recombinations of holes and electrons, Phys. Rev. 87 (1952) 835–842.
[20] D.O. Scalon, C.W. Dunnill, J. Buckeridge, S.A. Shevlin, A.J. Longsdail, S.M. Woodley, C.R.A. Catlow, M.J. Powell, R.G. Palgrave, I.P. Parkin, G.W. Watson, T.W. Keal, P. Sherwood, A. Walsh, A.A. Skol, Band alignment of rutile and anatase TiO_2, Nat. Mater. 12 (2013) 798–801.
[21] Z. Zhang, J.T. Yates, Band bending in semiconductors: chemical and physical consequences at surfaces and interfaces, Chem. Rev. 112 (2012) 5520–5551.
[22] X. Wang, Q. Xu, M. Li, S. Shen, X. Wang, Y. Wang, Z. Feng, J. Shi, H. Han, C. Li, Photocatalytic overall water splitting promoted by an α–β phase junction on Ga_2O_3, Angew. Chem. Int. Ed. 51 (2012) 13089–13092.
[23] H. Zhang, J.F. Banfield, Understanding polymorphic phase transformation behavior during growth of nanocrystalline aggregates: insights from TiO_2, J. Phys. Chem. B 104 (2000) 3481–3487.
[24] G. Liu, X. Yan, Z. Chen, X. Wang, L. Wang, G.Q. Lu, H.-M. Cheng, Synthesis of rutile–anatase core–shell structured TiO_2 for photocatalysis, J. Mater. Chem. 19 (2009) 6590–6596.
[25] J.-G. Li, T. Ishigaki, Brookite → rutile phase transformation of TiO_2 studied with monodispersed particles, Acta Mater. 52 (2004) 5143–5150.
[26] K. Sabyrov, V. Adamson, R.L. Penn, Two-step phase transformation of anatase to rutile in aqueous suspension, CrysEngComm 16 (2014) 1488–1495.
[27] H. Zhang, J.F. Banfield, New kinetic model for the nanocrystalline anatase-to-rutile transformation revealing rate dependence on number of particles, Am. Minerol. 84 (1999) 528–535.

[28] G. Li, L. Li, J. Boerio-Goates, B.F. Woodfield, High purity anatase TiO$_2$ nanocrystals: near room-temperature synthesis, grain growth kinetics, and surface hydration chemistry, J. Am. Chem. Soc. 127 (2005) 8659–8666.
[29] Z. Zhang, C.-C. Wang, R. Zakaria, J.Y. Ying, Role of particle size in nanocrystalline TiO$_2$-based photocatalysts, J. Phys. Chem. B 102 (1998) 10871–10878.
[30] S. George, S. Pokhrel, Z. Ji, B.L. Henderson, T. Xia, L. Li, J.I. Zink, A.E. Nel, L. Mädler, Role of Fe doping in tuning the band gap of TiO$_2$ for the photo-oxidation-induced cytotoxicity paradigm, J. Am. Chem. Soc. 133 (2011) 11270–11278.
[31] H. Zhang, J.F. Banfield, Phase transformation of nanocrystalline anatase-to-rutile via combined interface and surface nucleation, J. Mater. Res. 15 (2000) 437–448.
[32] H. Tian, J. Ma, K. Li, J. Li, Photocatalytic degradation of methyl orange with W-doped TiO$_2$ synthesized by a hydrothermal method, Mater. Chem. Phys. 112 (2008) 47–51.
[33] A.K. Chandiran, F. Sauvage, M. Casas-Cabanas, P. Comte, S.M. Zakeeruddin, M. Graetzel, Doping a TiO$_2$ photoanode with Nb^{5+} to enhance transparency and charge collection efficiency in dye-sensitized solar cells, J. Phys. Chem. C 114 (2010) 15849–15856.
[34] N.A. Deskins, M. Dupuis, Intrinsic hole migration rates in TiO$_2$ from density functional theory, J. Phys. Chem. C 112 (2008) 12981–12987.
[35] T. Luttrell, S. Halpegamage, J. Tao, A. Kramer, E. Sutter, M. Batzill, Why is anatase a better photocatalyst than rutile? Model studies on epitaxial TiO$_2$ films, Sci. Rep. 4 (4043) (2014) 1–8.
[36] B.-I. Park, H. Jie, B.-G. Song, K.-M. Kang, J.-K. Park, S.H. Cho, The structural morphological, and surface properties of tungsten-doped TiO$_2$ nanopowders and their contribution to the photocatalytic activity, Res. Chem. Intermed. 40 (2014) 115–126.
[37] S. Sathasivam, D.S. Bhachu1, Y. Lu, N. Chadwick, S.A. Althabaiti, A.O. Alyoubi, S.N. Basahel, C.J. Carmalt, I.P. Parkin, Tungsten doped TiO$_2$ with enhanced photocatalytic and optoelectrical properties via aerosol assisted chemical vapor deposition, Sci. Rep. 5 (10952) (2015) 1–10.
[38] N. Couselo, F.S.G. Einschlag, R.J. Candal, M. Jobbágy, Tungsten-doped TiO$_2$ vs pure TiO$_2$ photocatalysts: effects on photobleaching kinetics and mechanism, J. Phys. Chem. C 112 (2008) 1094–1100.
[39] T. Putta, M.-C. Lu, J. Anotai, Photocatalytic activity of tungsten-doped TiO$_2$ with hydrothermal treatment under blue light irradiation, J. Environ. Manag. 92 (2011) 2272–2276.
[40] M.M. Oliveira, D.C. Schnitzler, A.J.G. Zarbin, (Ti, Sn)O$_2$ mixed oxides nanoparticles obtained by the sol-gel route, Chem. Mater. 15 (2003) 1903–1909.
[41] R. Jenkins, R.L. Snyder, Introduction to X-ray Powder Diffractometry, Jonh Wiley and Sons, New York, 1996, p 90.
[42] B.K. Kaleji, Influence of co-doping of Sn/W on the structural and photocatalytic activity of TiO$_2$ nanoparticles for MB degradation, Opt. Quant. Electron. 47 (2015) 2075–2086.
[43] Y. Li, X. Zhou, W. Chen, L. Li, M. Zen, S. Qin, S. Sun, Photodecolorization of Rhodamine B on tungsten-doped TiO$_2$/activated carbon under visible-light irradiation, J. Hazard. Mater. 227–228 (2012) 25–33.
[44] P. Pu, H. Cachet, E. Ngaboyamahina, E. Sutter, Relation between morphology and conductivity in TiO$_2$ nanotube arrays: an electrochemical impedance spectrometric investigationJ, Solid State Electrochem. 17 (2013) 817–828.
[45] J. Ihm, A. Zunger, M.L. Cohen, Momentum-space formalism for the total energy of solids, J. Phys. C: Solid State Phys. 12 (1979) 4409–4422.
[46] W. Kohn, L.J. Sham, Self-consistent equations including exchange and correlation effects, Phys. Rev. 140 (1965) A1133–A1138.
[47] J.P. Perdew, K. Burke, M. Ernzerhof, Generalized gradient approximation made simple, Phys. Rev. Lett. 77 (1997) 3865–3868.
[48] S.L. Dudarev, G.A. Botton, S.Y. Savrasov, C.J. Humphreys, A.P. Sutton, Electron-energy-loss spectra and the structural stability of nickel oxide: an LSDA+U study, Phys. Rev. B 57 (1988) 1505–1509.
[49] G. Kresse, J. Hafner, Ab initio molecular dynamics for liquid metals, Phys. Rev. B 47 (1993) 558–561.
[50] J.P. Perdew, K. Burke, M. Ernzerhof, Generalized gradient approximation made simple, Phys. Rev. Lett. 781 (1997) 1396.
[51] J.P. Perdew, J.A. Chevary, S.H. Vosko, K.A. Jackson, M.R. Pederson, D.J. Singh, C. Fiolhais, Atoms, molecules, solids, and surfaces: applications of the generalized gradient approximation for exchange and correlation, Phys. Rev. B 46 (1992) 6671–6687.
[52] H.J. Monkhorst, J.D. Pack, Special points for Brillouin-zone integrations, Phys. Rev. B 13 (1976) 5188–5192.
[53] J. Heyd, G.E. Scuseria, M. Ernzerhof, Hybrid functionals based on a screened Coulomb potential, J. Chem. Phys. 118 (2004) 8207–8215.
[54] A.M. Márquez, J.J. Plata, Y. Ortega, J.F. Sanz, Structural defects in W-doped TiO$_2$ (101) anatase surface: density functional study, J. Phys. Chem. C 115 (2011) 16970–16976.
[55] C. Freysoldt, B. Grabowski, T. Hickel, J. Neugebauer, G. Kresse, A. Janotti, C.G. Van de Walle, First-principles calculations for point defects in solids, Rev. Mod. Phys. 86 (2014) 253–305.
[56] C.G. Van de Walle, J. Neugebauer, First-principles calculations for defects and impurities: applications to III-nitrides, J. Appl. Phys. 85 (2004) 3851–3879.
[57] M. Peressi, N. Binggeli, A. Balderreschi, Band engineering at interfaces: theory and numerical experiments, J. Phys. D 31 (1998) 1273–1299.
[58] D.R. Stull, H. Prophet, JANAF Thermochemical Tables, Natl. Bur. Stan. (U.S.), 2nd ed., GPO, Washington, DC, U.S, 1971.
[59] G.L. Humphrey, The heats of formation of TiO, Ti$_2$O$_3$ Ti$_3$O$_5$ and TiO$_2$ from combustion calorimetry 1, J. Am. Chem. Soc. 73 (1951) 1587–1590.